

Coincident locations of rupture nucleation during the 2019 Le Teil earthquake, France and maximum stress change from local cement quarrying

Vincenzo De Novellis¹, Vincenzo Convertito², Sotiris Valkaniotis³, Francesco Casu¹, Riccardo Lanari¹, Mario Fernando Monterroso Tobar¹ & Nicola Alessandro Pino²✉

Earthquake occurrence is ultimately controlled by tectonic stress load. Nevertheless, the 2019, $M_w = 4.9$, Le Teil earthquake in southern France occurred in an area where strain rates are relatively low. Human operations can produce increases in stress load and degradation of strength on nearby active faults, which raises the potential for failure. Here we present estimates of the rupture geometry and source directivity of the Le Teil earthquake based on differential synthetic aperture radar interferometry and seismic data. We find that almost two centuries of mass removal at a nearby cement quarry likely provided the required stress change to hasten the occurrence of the Le Teil earthquake by more than 18,000 years. We suggest that further mass removal in the area might lead to even stronger earthquakes, by activating deeper sectors of the same fault plane.

¹ Consiglio Nazionale delle Ricerche, Istituto per il Rilevamento Elettromagnetico dell'Ambiente, Napoli, Italy. ² Istituto Nazionale di Geofisica e Vulcanologia, Osservatorio Vesuviano, Napoli, Italy. ³ Koronidos Str., 42131 Trikala, Greece. ✉email: alessandro.pino@ingv.it

Regional and local stress conditions driven by tectonic forces and, in particular, the value of the differential stress on the fault drives the occurrence of earthquakes. Nevertheless, large scale industrial activity might result in stress variation large enough to induce earthquakes or—added to the tectonic stress—to overcome the fault strength, advancing the time to the next expected rupture. Physical processes commonly considered capable of inducing or triggering seismic events by anthropogenic activities include underground volumetric changes, fluid pressure diffusion with/without fluid flow in rock fractures/pores, and thermal stress variations due to temperature gradients (e.g., ref. 1–7). Besides, a very limited number of cases also report about causal relationship between earthquakes and mass removing from Earth's surface, related to quarry activity^{2,8–10}.

On November 11, 2019, an $M_W = 4.9$ earthquake rocked southeastern France, close to the small town of Le Teil and about 10 km from Montelimar. Four people were injured and hundreds of buildings damaged, some of which collapsed. The earthquake happened in the proximity of the NE–SW, southeast-dipping, St. Thomé-La Rouvière fault (LRf) system¹¹, which marks the southeastern border of the Massif Central over almost 150 km¹², in an area where intense rock extraction has been proceeding since the eighteenth century. The fault system is associated with the Variscan orogeny (more than 280 Ma) and during the Oligocene age (about 30 Ma) was characterized by extensional tectonics¹³. The region is characterized by a very low seismic activity rate, with maximum magnitude ranging between 3 and 4, as deduced from the seismic catalog of the French national seismic network RéNaSS (<https://renass.unistra.fr/recherche>; last accessed April 2020). Important historical earthquakes occurred in 1773 and 1873, about 30 km S–SE of Le Teil, with maximum intensity level I_{MAX} VIII¹⁴. The current phase of tectonic deformation in the area, starting ~20 Ma, is characterized by NW–SE compression, coherent with the 140° direction indicated by the World Stress Map (<http://www.world-stress-map.org>; last accessed July 2020), and associated with a relatively low strain rate $\sim 0.5 \times 10^{-9}$ year⁻¹ (ref. 15–17). Nevertheless, no evidence of cumulate compressional deformation has been detected along the ruptures associated with the 2019 earthquake and, remarkably, the geologic evidences suggest that the La Rouvière fault could have been inactive since million years¹⁸.

Based on the above piece of evidence, we analyzed the source characteristics of the Le Teil earthquake and investigated the possible link with the nearby industrial activities. Our results indicate that the extraction activity could have triggered the Le Teil earthquake. In this case, we estimate a clock advance larger than 18,000 years.

Results

Geodetic data inversion. Hypocentral locations for the 2019 event provided by different institutions are quite scattered. The ones better constrained, being obtained from regional—rather than teleseismic—first arrivals travel times, are located a few kilometers southwest of Le Teil, at a depth shallower than 5 km (Fig. 1a; Table 1). The epicentral area is characterized by an intricate structural setting, with several faults trending approximately NE–SW, interconnected with minor NW–SE structures^{11,12}. Coseismic ground ruptures¹⁸ (Fig. 1b) have only been detected along the northern end of LRf, close to Le Teil, where it trends about N50°. The fault mechanisms issued by French and international institutions (Fig. 1b; Table 1) indicate compressive source kinematics associated with a NE–SW trending plane, compatible with both the azimuth of the major faults in the area and the local stress field. The observed surface effects are located 1–2 km E–SE from the instrumental epicenters and are proximal to a large quarry complex where large volumes of limestone have been

continuously removed for almost two centuries. This circumstance, along with the very low rate of seismicity in the region, raised public concern about the possible anthropogenic origin of the earthquake (e.g., <https://www.nationalgeographic.com/science/2019/11/weird-earthquake-crack-france-geologists-buzzing/>), in particular regarding extraction activities in the Le Teil quarry, located only 1 km east of the surface ruptures (Fig. 1a, b).

We used space-borne differential synthetic aperture radar interferometry (DInSAR) measurements to derive the static ground displacements caused by the Le Teil earthquake. The deformed surface (Fig. 2) is elongated in the NE–SW direction, similar to the orientation of the LRf, with an extent of about 12 km². Clear ground uplift results on the SE side of LRf, with a maximum over 10 cm, while a general subsidence results across the fault, with a slightly smaller maximum with respect to the uplift. Notably, a clear asymmetry is evident in the northern sector of the deformed zone, in correspondence of a minor fault located at the base of La Chade Hill's NW flank¹², calling for a more complex geometry of the ruptured area. Thus, to model the source geometry, we computed the analytical solutions for shear dislocation in an elastic and homogeneous half-space¹⁹, reproducing the coseismic surface deformation associated with the Le Teil earthquake. Our preferred solution (see “Methods” section and Supplementary Table 1) is characterized by almost pure reverse faulting on two distinct surfaces, $F1$ and $F2$, with an area smaller than 3.5×1.9 km² and 1.8×1.9 km², respectively (Fig. 2). $F1$ strikes 43.2°, with dip 52.1°, and coincides with the central sector of the LRf, while $F2$, oriented at 25.4° and dipping 68.1°, is located slightly northeast of $F1$ and exactly corresponds with the La Chade Hill fault (LCF). Both model dislocations are located within 1 km from the surface and the distributed slip model features two main slip patches, one on each of the two planes. The maximum slip values are 0.29 m and 0.21 m, respectively for $F1$ and $F2$, both located at depth of about 0.7 km.

Source directivity analysis. It is worth noting that the instrumental hypocentral locations do not appear to be compatible with the causative faults resulting from the geodetic modeling. Thus, in order to get a deeper understanding of the earthquake source, we also investigated the source directivity by analysing the spectrum apparent corner frequency of the seismograms recorded at 16 stations within 300 km from the source, at different azimuths. A bilateral rupture results, with the dominant direction at $241 \pm 8^\circ$ and a secondary one at about 60° , associated with considerably lower seismic moment release (see “Methods” section). Moreover, the ratio between the rupture velocity v_r and the S-wave velocity is 0.5 ± 0.1 , which indicates a rather slow rupture propagation velocity. These results put clear constraints on the location of the nucleation point, implying that the rupture likely nucleated either on the northern end of $F1$ or on the southern end of $F2$, i.e., in between the two main slip patches and about 1 km east of the instrumental epicentral locations (Fig. 1), and propagated on the two planes in opposite directions, at very shallow depth (within approximately 1 km). This latter feature is usually associated with seismicity induced/triggered by anthropogenic activity^{1,2,20}

Estimation of the mass removal. The documentation of the possible link between the earthquake and the mass removal from the close Le Teil quarry requires a volume estimate of the mass removed from the Earth's surface since the beginning of the extraction activity in 1833. To this aim, we reconstructed the topographic changes of the Le Teil quarry area by developing digital surface models (DSM) at various dates (Fig. 3a; see “Methods” section). To increase coherency and avoid large

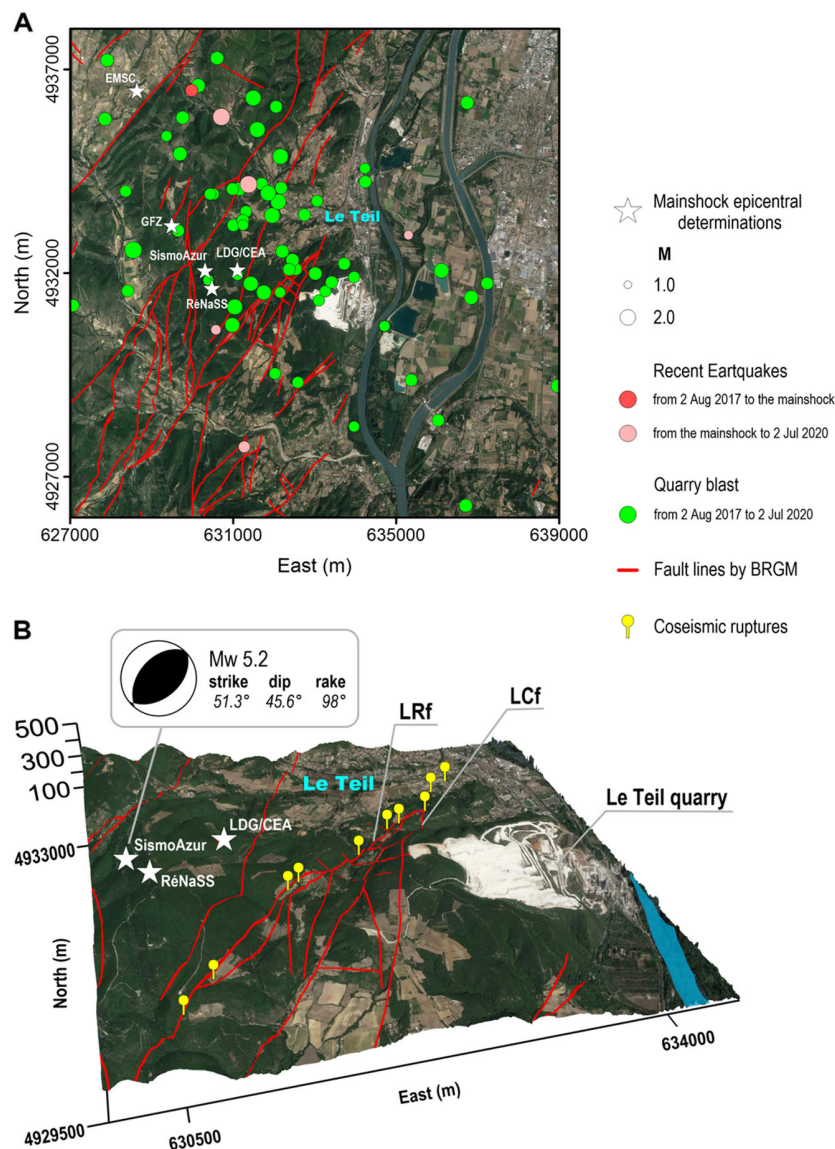


Fig. 1 The 2019 Le Teil earthquake. **a** Map showing distinct locations of the 2019 earthquake (Table 1), quarry blasts and earthquakes from the RéNaSS catalog (<https://renass.unistra.fr/recherche>; last accessed April 2020), and the main geological lineaments¹². **b** Perspective view with indication of the La Rouvière (LRf) and La Chade (LCf) faults, and coseismic ground ruptures¹⁸. The mechanism from SismoAzur (Table 1) is also reported. Both images are as of August 25, 2018.

outliers, we split the whole period into a few intervals. We used archive stereo aerial image pairs from the Institut National de l'Information Géographique et Forestière (IGN), for 1946, 1979, 2007, and 2011, the most recent available. In order to recreate the pre-extraction topography of the site, we used the Carte de l'État-Major that dates back to 1846–1857, the earliest available topographic map of a suitable scale (1:40,000). We determined the volume extracted up to 2011, during the distinct time periods, from the comparison of the point clouds extracted from the topographic data (Fig. 3b). The rate of volume removal has been increasing dramatically through time—also thanks to the technological progress—from about 100,000 m³/year, operated up to the middle twentieth century, to more than 1,000,000 m³/year, i.e., more than one order of magnitude, with a substantial acceleration in the last decades (see “Methods” section).

Stress change caused by the quarry activity. We attempt to quantify the stress change induced on the faults associated

with the 2019 earthquake by the mass subtracted from the Le Teil quarry. For each analyzed time interval we estimated the equivalent vertical force distribution corresponding to the total extracted rock, with a grid spacing of 2 m, and used the Boussinesq's solution of three-dimensional elastostatics to compute the stress change in terms of Coulomb failure function variation, $\Delta CFF = \Delta\tau + \mu'\Delta\sigma_n$, on both model faults (Fig. 3c).

The cumulative ΔCFF is characterized by relatively large areas of high stress increase on both of the considered faults. In particular, a large patch of stress increase resulted on the northern half of the LRf, with maximum corresponding to 0.19 MPa, while the Coulomb stress increased on most of the LCf, reaching a maximum change of 0.18 MPa. These values are less than one order of magnitude smaller than the stress drop $\Delta\sigma = 1.3$ MPa estimated for the 2019 earthquake (see “Methods” section). Remarkably, (1) the portions of the causative faults where the slip distribution resulting from the inversion of the geodetic data displays a locked segment at the surface (southern end of the LCf

Table 1 Source parameters provided by several institutions for the November 11, 2019, Le Teil earthquake.

Source	East (m)	North (m)	Depth (km)	M_w	M_0 (N m)	Strike (°)	Dip (°)	Rake (°)
EMSC ^a	628,632.45	4,936,461.02	10	4.9				
GFZ ^b	629,493.01	4,933,144.44	10	4.9	2.5×10^{16}	27	49	83
INGV ^c	627,327.13	4,921,989.49	9	4.9	2.7×10^{16}	50	37	102
USGS ^d	629,968.05	4,941,154.90	10	4.8	2.3×10^{16}	53	57	99
LDG/CEA ^e	631,104.33	4,932,065.56	2	4.8	2.2×10^{16}	62	59	107
RéNaSS ^f	630,477.61	4,931,608.43	2	5.2 ^g				
SismoAzur ^h	630,309.76	4,932,040.56	3	4.8	2.1×10^{16}	51.3	45.6	98

All the hypocentral locations are from first arrivals travel times.
^aEMSC catalog (<https://www.emsc-csem.org/#2>; last accessed April 2020).
^bGFZ catalog (<https://geofon.gfz-potsdam.de>; last accessed April 2020).
^cLocation from INGV catalog (<https://cnt.rm.ingv.it>; last accessed April 2020); M_w , M_0 , and focal mechanism from INGV-Regional Centroid Moment Tensor Project (<https://rcmt2.bo.ingv.it>; last accessed April 2020).
^dUSGS catalog (<https://earthquake.usgs.gov/earthquakes/search/>; last accessed April 2020).
^eLDG/CEA catalog (http://www-dase.cea.fr/actu/dossiers_scientifiques/2019-11-11/index.html; last accessed April 2020).
^fRéNaSS catalog (<https://renass.unistra.fr/recherche>; last accessed April 2020).
^g M_c .
^hSismoAzur catalog (<http://sismoazur.ocu.eu/catalog>; last accessed April 2020).

and northern end of the LRF) are associated with areas of negative or almost zero Coulomb stress change, and (2) the overall stress increase area is located right in between the two fault planes, in the middle of the major slip patches (Fig. 2). When considered with the result of the directivity analysis, this evidence further supports the location of the rupture nucleation in the central part of the surface deformed area, on any of the two planes, i.e., where the surface mass removal caused the maximum stress change (Fig. 3c, and about 1 km east of the epicentral location resulting from first arrival travel times (Table 1).

Discussion

Overall, our results pose specific questions on the possible effects of the anthropic activity on the earthquake occurrence. In particular, (1) did the mass removal induce or trigger the earthquake and, (2) in the latter case, what is the clock advance with respect to the time the event would have occurred under the tectonic stress load alone? The tectonic horizontal strain (shortening) rate in the area is $\sim 0.5 \times 10^{-9} \text{ year}^{-1}$ (ref. 15–17), oriented N140°. By considering only the LRF, releasing most of the seismic moment during the Le Teil earthquake, this suggests that an earthquake on this fault could have occurred anyway sometime in the future but the quarry activity triggered it, hastening its occurrence. There is no information on past seismic events on this fault and no speculation can be done on the possible recurrence time of sizeable earthquakes associated with it. However, by assuming an average rigidity of $G = 32 \text{ GPa}$ for the crust, the horizontal stressing rate $\dot{\sigma} = G\dot{\epsilon}$ associated with the mentioned shear strain rate $\dot{\epsilon}$ would be $\sim 15 \text{ Pa/year}$. By considering the single plane solution, the projections of this stress rate on the fault correspond respectively to $\sim 13 \text{ Pa/year}$ and $\sim 6 \text{ Pa/year}$ for the normal σ_n and shear τ stress components. The estimated cumulative maximum Coulomb stress change on the fault due to the total mass subtraction is 0.19 MPa by 2011, corresponding to maximum normal $\Delta\sigma_n = 0.21 \text{ MPa}$ and shear stress $\Delta\tau = 0.11 \text{ MPa}$. By accounting for the uncertainty in the estimated volumes (see “Methods” section), these stress values can be considered reliable within $\pm 10\%$. Noteworthy, considering that about 10% of the total stress change derives from the mass removal in 1833–1946, the larger uncertainty associated with the reconstruction of the initial reference topography (see Methods and Supplementary Information), would only affect the final stress calculation by $< 5\%$.

The shear stress value resulting from the quarry activity is one order of magnitude larger than what is typically considered sufficient to trigger an earthquake (0.01 MPa), pointing to an

anthropogenic effect on the origin of the seismic event²¹. In fact, these results allow stating that the rock extraction from the quarry likely have triggered the 2019 Le Teil earthquake by dramatically accelerating the loading of the fault and hastening its unlocking. Incidentally, we note that even considering the upper extreme for the stress drop ($\Delta\tau = 2.0 \text{ MPa}$, see “Methods” section), this would not change our conclusion and the hypothesis of a significant anthropogenic effect on the origin for the earthquake still holds.

The time advance can be estimated by dividing the cumulative stress change associated with the quarry activity by the tectonic stress rate²². About 18,000 years is the time required for the tectonic forces to load on the fault a stress amount similar to the change produced by ~ 180 years of rock extraction from the quarry (Fig. 4). However, in this computation we did not include the mass removal relative to the period 2011–2019—because this information is not available to us—thus the above conclusions represent a conservative estimate. Assuming for 2011–2019 the same average extraction rate calculated for the period 2007–2011 (and the same location), the total normal and shear stress change would be $\Delta\sigma_n = 0.26 \text{ MPa}$ and $\Delta\tau = 0.15 \text{ MPa}$, respectively, corresponding to a time advance of $\sim 25,000$ years, making the triggering hypothesis even more realistic. Considering the remarkable increase in the number and the magnitude of the quarry blasts in the area in the last few years (Supplementary Fig. 1), the recent extraction rate could have been even higher than what assumed and the estimated stress load would be larger.

In addition to the static stress change, the above results cannot exclude that the dynamic shaking from the quarry blasts possibly could have had a role in contributing to trigger the event, either in terms of short-term dynamic stress (due to transient stress perturbation) or by material fatigue due the repeated shaking.

Finally, the unusual aspect ratio and the very shallow distribution of the coseismic slip, very similar to other cases of triggered earthquakes²³, could be interpreted as an indication that the stress change associated with the quarry extraction was enough to overcome the fault strength at shallow depth, but not sufficient to exceed the fault resistance deeper than that. In this hypothesis and especially if on deeper portions of the fault there is near-critical preexisting tectonic stress, additional future mass removal might trigger deeper slip, possibly causing a stronger earthquake than the one that occurred on November 11, 2019.

Methods

DInSAR data analysis. In order to investigate the ground displacements associated with the considered seismic event, we exploited the Differential Synthetic

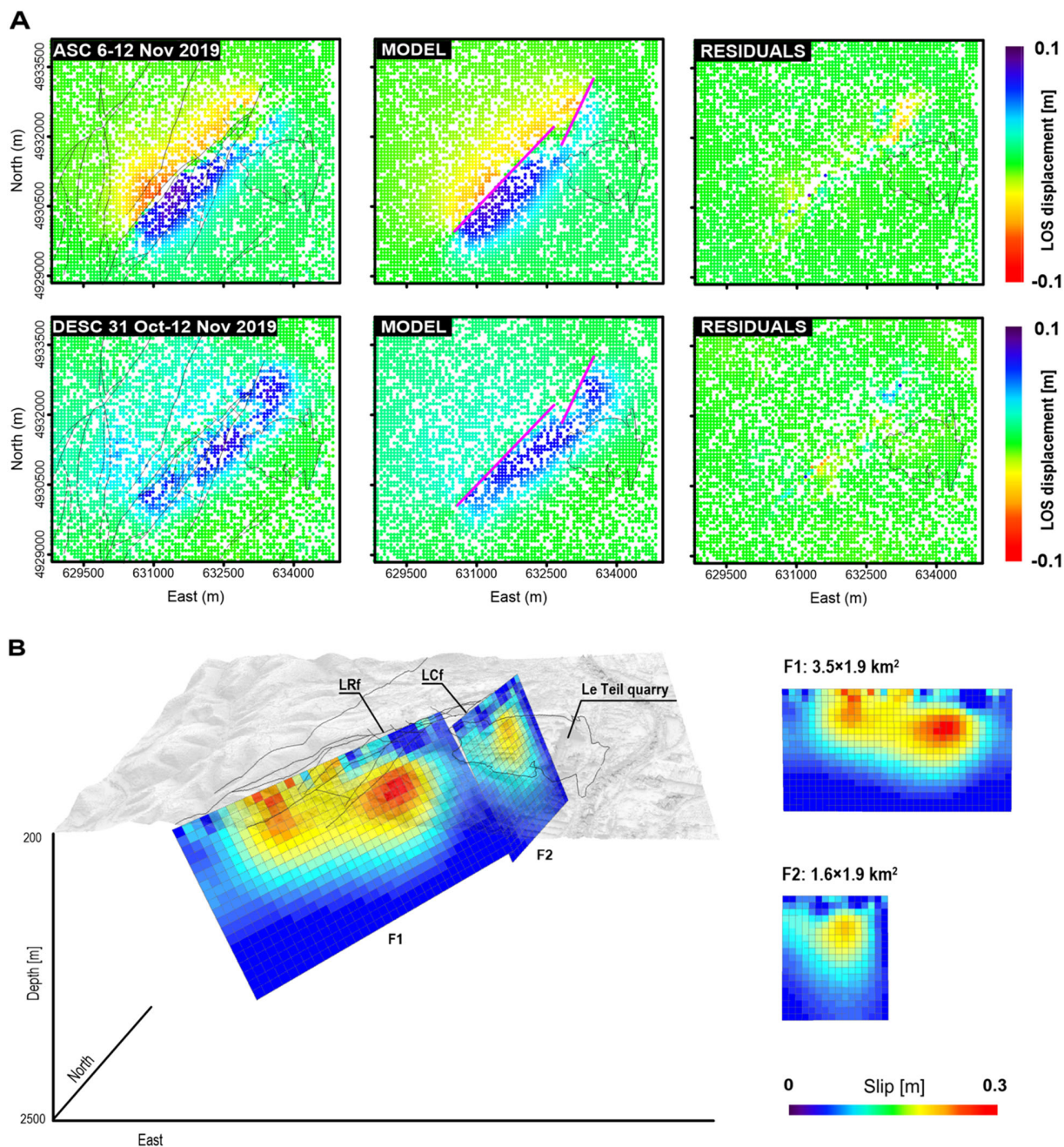


Fig. 2 Modeling of the DInSAR data. **a** Data, modeling results, and residuals for line-of-sight surface displacement for ascending (ASC) and descending (DESC) orbits DinSAR interferograms. The fault trace of the two retrieved rupture planes is indicated by magenta lines, while the black contour depicts the Le Teil quarry. **b** The dislocation resulting from the inversion of the ground deformation data is displayed in both perspective and plane view. Each pixel is 100 × 100 m².

Aperture Radar (SAR) Interferometry (DInSAR) technique, which allows the analysis of surface displacements along the radar line-of-sight (LOS). The SAR data considered were acquired by the Sentinel-1 (S1) constellation of the Copernicus European Program. Benefiting from the short revisit time and the small spatial baseline separation of the S1 constellation, we generated several coseismic differential interferograms (Supplementary Table 2) with a spatial sampling of about 15 m following an averaging operation (multilook) in the azimuth direction to reduce the speckle noise. Among the generated interferograms we selected those less affected by undesired phase artifacts (atmospheric phase delays, decorrelation noise, etc.) for the seismic source modeling discussed in the following section, thus preserving good spatial coverage and interferometric coherence. In particular, the employed S1 data pairs were acquired on November 6–12, 2019 (Supplementary Fig. 2A), and on October 31 and November 12, 2019 (Supplementary Fig. 2B) along the ascending (ASC) and the descending (DESC) orbits, respectively. On

both interferograms, several fringes located near the epicentral area are clearly visible; note that each fringe corresponds to a LOS displacement of about 2.8 cm (i.e., half of the employed S1 C-band wavelength $\lambda = 5.546$ cm). Subsequently, starting from the selected interferograms, we generated their corresponding LOS displacement maps (Fig. 1a) through a phase unwrapping operation²⁴.

By superimposing the fault traces on the selected pair of interferograms (Supplementary Fig. 2C, D and Fig. 1d) it is evident that the deformed area, extending for about 12 km², is elongated in the NE–SW direction, very similar to the orientation of the LRf. Moreover, a clear asymmetry is clearly visible in the northern sector of the deformed zone, in correspondence of a minor fault located at the base of La Chade Hill’s NW flank (Supplementary Fig. 2E, F), suggesting a complex geometry of the ruptured area. This is also evident in the map of the vertical component of the retrieved deformation pattern (Supplementary Fig. 3A) that we computed from the unwrapped interferograms, together with the East-

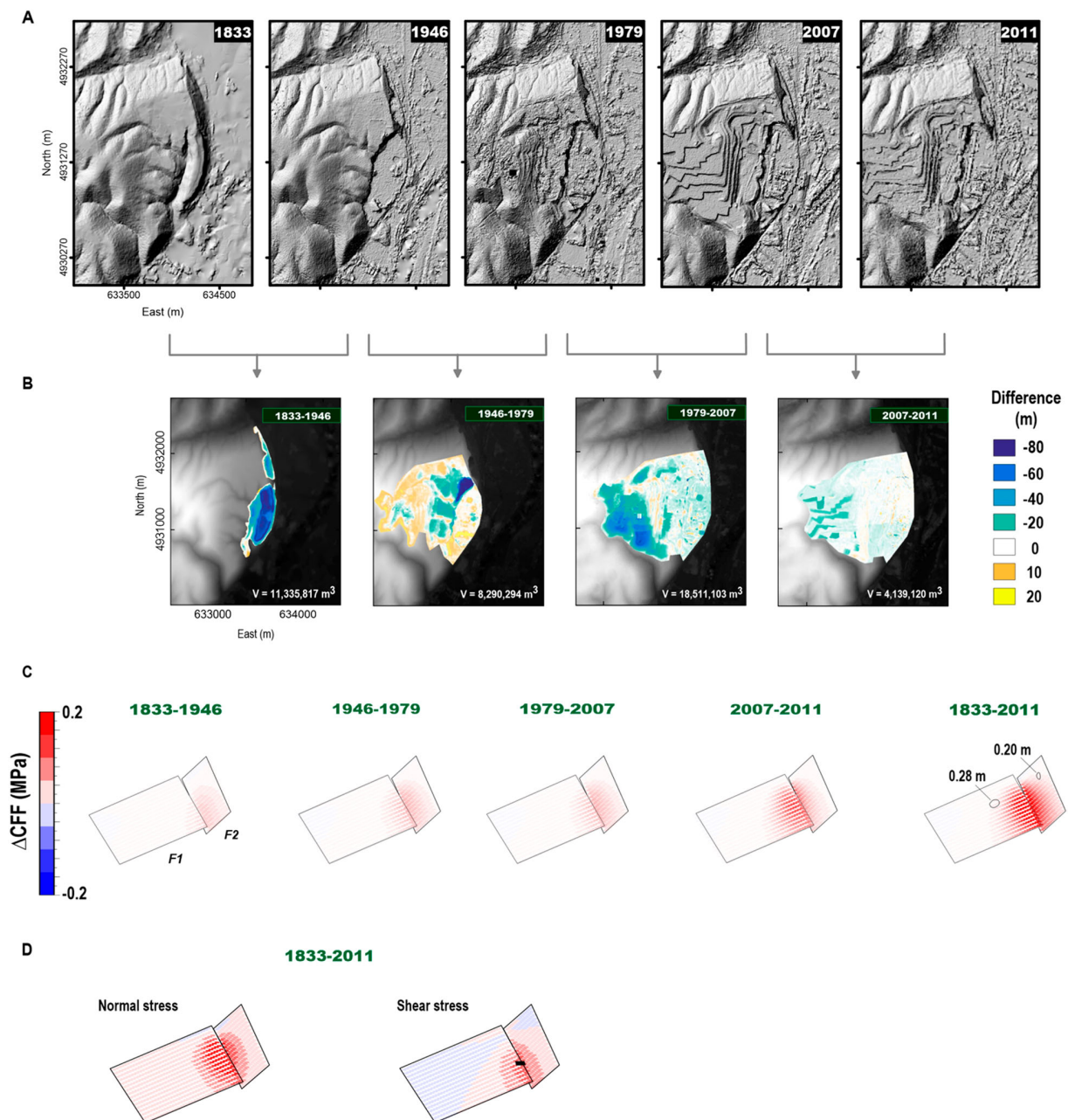


Fig. 3 Estimate of the volume removed from the quarry and Coulomb stress modeling. **a** Digital Surface Model (DSM) of the considered area at successive times. **b** Computation of the rock volumes retrieved by numerically comparing the available DSM. **c** Coulomb stress change, computed for $\mu' = 0.4$, caused by the mass removed from the Le Teil quarry on the fault planes associated with the 2019 earthquake. The black contours in the rightmost panel outline the area with coseismic slip larger than 0.28 m for *F1* and larger than 0.20 m for *F2*. **d** Normal and shear stress components of the Coulomb stress change for the whole analyzed period. The small black square indicates the point where the shear stress illustrated in Fig. 4 is computed.

West deformation map (Supplementary Fig. 3B). Note that the maximum uplift is about 11 cm while the amplitude of the subsidence is appreciably smaller, with a maximum displacement of about 4 cm. For the horizontal displacements, the area affected by westward motion is rather extended, with a maximum value of about 8 cm, while eastward motions are more concentrated on the SW side of the LRF and shows a maximum displacement of about 7 cm.

Surface deformation data modeling. In order to retrieve the fault parameters, we jointly inverted the DInSAR displacements retrieved from ASC and DESC orbits by applying a consolidated two-step approach that consists of a nonlinear optimization to constrain the fault geometry, assuming a uniform slip, followed by a linear inversion to retrieve the slip distribution on the fault plane²⁵. We modeled the LOS

displacements retrieved from the DInSAR interferograms with a finite rectangular dislocation in an elastic and homogeneous half-space¹⁹, also applying a compensation for the local topography²⁶ and assessing possible offsets and linear ramps affecting the DInSAR measurements. Moreover, data were preliminarily resampled over a regular grid (70 m spacing in all the considered area) to reduce the computation load. Starting from a nonlinear inversion algorithm based on the Levenberg–Marquardt least-squares approach, we searched for the source parameters of one or two rectangular dislocations with uniform slip and, thanks to multiple random restarts implemented within the approach, it was possible to catch the global minimum during the optimization process.

The second step of our modeling is represented by the linear inversion process with the computation of the nonuniform slip distribution, in order to have a more accurate estimate of the slip distribution along the fault plane. In particular, the

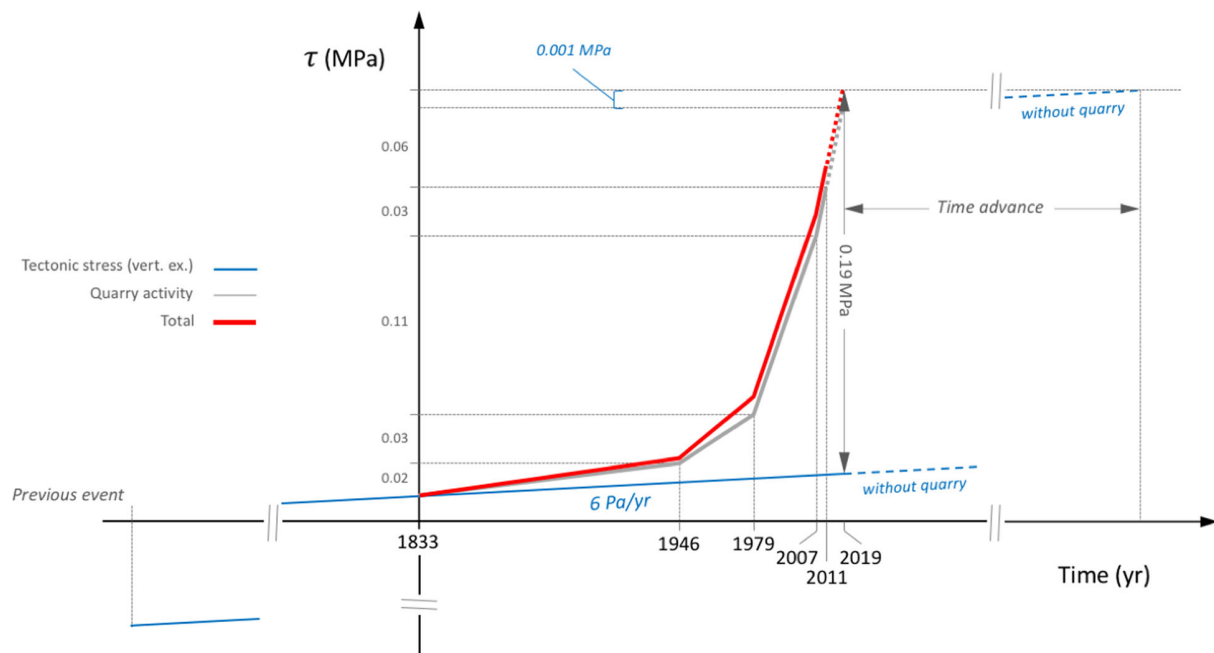


Fig. 4 Stress progression on the main fault. The increment of the shear stress on the faults of the 2019 earthquake caused by the tectonic forces (blue line; exaggerated vertical scale), starting from the previous (unknown) earthquake, and by the Le Teil quarry activity (0.19 MPa; gray line). The anthropogenic shear stress is computed at the point marked by the small black square in Fig. 3. The total shear stress on the fault is represented by the red line. The horizontal gray line on top marks the fault strength.

linear inversion was performed by using as starting model, in terms of dimensions and orientation, the fault obtained from the previous nonlinear inversion discretized into $0.1 \times 0.1 \text{ km}^2$ patches and inverting the following system:

$$\begin{bmatrix} \mathbf{d}_{\text{DInSAR}} \\ 0 \end{bmatrix} = \begin{bmatrix} \mathbf{G} \\ \mathbf{k} \cdot \nabla^2 \end{bmatrix} \cdot \mathbf{m},$$

where $\mathbf{d}_{\text{DInSAR}}$ represents the DInSAR displacements vector, \mathbf{G} is the Green's matrix with the point-source functions, \mathbf{m} is the vector of slip values for each patch (initially assumed as the value resulting from the nonlinear inversion), and ∇^2 is a smoothing Laplacian operator weighted by an empirical coefficient k to guarantee a reliable slip varying across the fault. The choice of the parameter k depends on the compromise between the data fit and the smoothness of the slip distribution. We tested several values and selected $k = 0.007$, since appreciably higher residuals resulted for $k \geq 0.01$ and similar residuals but inconsistent slip values (larger than 70 cm), with too rapidly varying slip distribution, resulted for $k \leq 0.004$. Further constraints were introduced by imposing nonnegative slip (reverse slip only) values obtained via nonlinear inversion.

The surface deformation derived from the interferometric measurements acquired along ASC and DESC orbits reveals a spoon-like geometry, characterized by a NE-SW striking main distinctive displacement pattern (Supplementary Fig. 2). Thus, we first investigated solutions associated with homogeneous dislocation on a single planar source for which all source parameters were set free during the nonlinear inversion. Then, keeping the plane obtained in the geometry inversion fixed, we searched for the best slip distribution. The preferred solution (Supplementary Table 1) consists of a $4.1 \times 1.0 \text{ km}^2$ reverse fault, oriented N50° and dipping 62.3° southeast, with rake 116.5° and dislocation characterized by two separate major patches, located respectively north and south of the quarry, with a maximum slip in excess of 0.3 m (Supplementary Fig. 4). Although the single fault solution accounts for most of the observed DInSAR data, it is associated with large residuals, comparable to the maximum surface deformation (Supplementary Fig. 4). Also, it is worth noting that this solution does not align with any, and actually crosscuts all the faults mapped in the area. Thus, considering these observations, we tested a composite solution, with two fault planes. Similar to what was done for the single fault, we first searched for the best geometry for the two planes, by means of nonlinear inversion with uniform dislocation, and then solved for the slip distribution on the two fault surfaces with fixed geometry by linear inversion. Based on the features of the DInSAR data described above and on the local geology^{11,12}, we tested several positions for the two faults in the uniform slip, nonlinear inversion, always keeping free strike, dip, rake (uniform for each plane), and dislocation. Eventually, we obtained solutions (Supplementary Table 1) noticeably reducing the residuals and, most importantly, compatible with the faults observed at the surface (Fig. 2b and Supplementary Figs. 2 and 3). The two planes

coincide respectively with the central sector of LRF and to a structural lineament at the base of the La Chade Hill, both supposed to be SE dipping¹¹, where the quarry is located. The preferred solution is characterized by a slip distribution shallower than 1 km depth. In particular, for the plane *F1* the solution displays a 3 km-long, two-lobed patch with maximum slip of 0.29 m located on the northern half of the fault, while a maximum slip of 0.21 m results for *F2*, located approximately at the center of the fault.

Finally, as for the uncertainties associated with the slip solution we report the standard deviation (Supplementary Fig. 5) as obtained from the model covariance matrix, following an approach²⁵ that accounts also for the noise covariance.

Source directivity analysis and stress drop estimate. We studied source directivity by using a simplified version of the directivity function C_d (ref. 27) for a bilateral linear rupture model:

$$C_d = \frac{1}{2} \sqrt{\frac{(1+e)^2}{(1-\alpha \cos \vartheta)^2} + \frac{(1-e)^2}{(1+\alpha \cos \vartheta)^2}}, \quad (1)$$

where ϑ is the angle between the ray leaving the source and the direction of rupture propagation φ (ref. 28), and α is the Mach-number, that is, the ratio between the rupture velocity v_r and the S-wave velocity. The percent unilateral rupture e parameter is defined as $(2L' - L)/L$, where L is the total rupture length and L' is the length of the dominant rupture²⁹. A value of $e = 1$ corresponds to a unilateral rupture, whereas $e = 0$ corresponds to a bilateral rupture.

The effect of the directivity on the source spectrum is to increase the corner frequency at those stations located in the same direction as the rupture propagation and to decrease the corner frequency in the opposite direction (e.g., ref. 30). This effect can be modeled assuming that the apparent corner frequency is given by $f_{ca} = f_c C_d$ with f_c indicating the actual corner frequency and f_{ca} the corner frequencies at various azimuths estimated from the source spectrum.

We retrieved waveforms corrected by the instrumental response at 22 stations from the Réseau Sismologique et Géodésique Français (<http://seismology.resif.fr/#WelcomePlace>; last accessed April 2020) (Supplementary Fig. 6A). We filtered all the waveforms in the frequency band 0.01–20 Hz. First, we discarded the stations with a low signal-to-noise ratio, which resulted to be poor at all the stations located at an elevation higher than 900 m, reducing the number of stations to 16. Then, we windowed the waveforms by cutting from 2 s before the manual S-wave picking to 6 s after. We applied a 5 per cent cosine taper function and zero padding before computing the Fourier amplitude spectra. The spectra were then smoothed by applying an average moving window with a four-point half width. Finally, we computed the S-wave displacement spectra from the modulus of the three components velocity or acceleration spectra by dividing the spectra by 2π or $4\pi^2$, respectively.

We assumed an ω^{-2} theoretical source spectrum model³¹, which is given by:

$$S(f) = \frac{\Omega_0}{1 + \left(\frac{f}{f_c}\right)^2}, \quad (2)$$

where Ω_0 is the long-period spectral amplitude, f the frequency, f_c the corner frequency. As for the anelastic attenuation we assumed the model $A(f, T) = e^{-\pi f T / Q(f)}$, where $Q(f) = Q_0 f^n$ and T is the travel time of the S phase. Using Eq. (2), together with the attenuation model, we fit the observed spectra through a grid search approach, to infer Ω_0 , f_c , Q_0 and n . As for Ω_0 , we normalized the spectrum and explored the range (0.7, 1.3), while the range of exploration for f_c was (0.1, 2.0). Finally, we explored Q_0 in the range (0, 300) and n in the range (0, 2.0). The parameter Ω_0 is then used to compute the seismic moment³² through the formulation:

$$M_0 = \frac{4\pi\rho c^3 R \Omega_0}{FR_{\theta_{\phi}}},$$

where R is the hypocentral distance, ρ is the density, assumed here 2690 kg m^{-3} , and c is S -wave velocity assumed to be 3.5 km s^{-1} . $R_{\theta_{\phi}}$ is the average S -wave radiation pattern assumed to be 0.7 and F is the free-surface coefficient (fixed to 2). As for the uncertainty on each inferred parameter we used an approach³³ providing confidence intervals based on jack-knife variance analysis. The computed f_c as function of the station azimuth are finally fit by using the C_d function and the nonlinear Levenberg–Marquardt least-squares algorithm.

The observed displacement spectra together with the best-fit models are shown in the upper panels of Supplementary Fig. 6B. The average seismic moment value is 3.4×10^{16} (2.4×10^{16} , 4.9×10^{16}) N m corresponding to $M_w = 4.9$. As for the anelastic attenuation, we found that a Q frequency independent model (i.e., $n = 0$) provides the best fit, with $Q_0 = 190$ (193, 198). The estimated corner frequencies are shown in the lower panel of Supplementary Fig. 6B as a function of the station azimuth. The result clearly indicates at least one range of azimuths where the f_c value increases with respect to the other directions. The fit with the C_d function, which is shown in the same panel, provides an e -value of 0.3 ± 0.1 indicating a bilateral rupture and a Mach-number of 0.5 ± 0.1 suggesting a rather low rupture propagation. The dominant rupture direction is at $241 \pm 8^\circ$ while the secondary direction is at about 60° . Using the average value of the estimated corner frequencies corresponding to 0.6 (0.5, 0.7) Hz and the seismic moment, we computed the static stress $\Delta\sigma = 0.44 M_0/r^3$, with the source radius given by $r = 0.37 v_s/f_c$ (ref. 28), being v_s the S -wave velocity. We obtained $r = 2158$ (2044, 2846) m and $\Delta\sigma = 1.3$ (0.9, 2.0) MPa.

Calculation of the rock volume extracted from the quarry. We used multi-temporal DSM to estimate the removed volume of rock in the Le Teil quarry. Topographic map resolution, quality, and accuracy varies a lot with time, so a more robust method of change detection using high-resolution topography from stereo aerial imagery is preferred. However, the Le Teil quarry was established in 1833 and this technique is only available for the modern era. Thus, distinct methods must be used for the different time periods.

For the recent period, we used scanned stereo aerial images of the study area, available from the Institut National de l'Information Géographique et Forestière (IGN). We used archive stereo aerial image pairs for 1946, 1979, 2007, and 2011 (Supplementary Table 3). We extracted DSM from stereo imagery using MicMac software³⁴, following the procedure illustrated in Supplementary Fig. 7. For each group of stereo images, tie-points between images and camera frame/lens parameters were calculated. Using ground control points, we performed bundle adjustment and refinement of the camera calibration. Ground control points were picked from the latest IGN orthophoto map (coordinates in UTM zone 31 north, WGS84) and elevation values were extracted from ALOS Global Digital Surface Model. Then, DSM and orthophotos were produced. A point cloud was extracted from the Malt DSM and colored with RGB values from the orthophoto map (Supplementary Fig. 7). A detailed photogrammetric point cloud of 2007 covering a much larger area is available from the OpenTopography facility (<https://doi.org/10.5069/G9BC3WQ4>; last accessed April 2020).

Incidentally, we remark that there is a strip of images dated 1932 available from IGN, but processing produced many artifacts due to scanned film's poor preservation and noise. Coregistration with 1946 data was also poor, with large residuals; thus, we decided not to use the 1932 dataset. We did not use the most recent set of digital aerial images provided by IGN (dated 2013), as the poor radiometric quality of the files leads to a low quality matching over the quarry area, thus rendering the dataset unusable for terrain change detection.

In order to estimate the initial reference topography of the site as best as possible, we searched for the earliest available topographic map on a suitable scale. We used the Carte de l'État-Major-feuille Privas S.O. (Supplementary Fig. 8), a map compiled between 1846 and 1857 at a scale 1:40,000. We georeferenced a high-resolution scan obtained from IGN (<https://www.geoportail.gouv.fr/donnees/carte-de-letat-major-1820-1866>; last accessed April 2020). A concise description of the main map-series features and how to spatially process each map sheet is also available³⁵. As the map does not provide detailed and accurate contour lines, we extracted a dense set of elevation contours from the 1946 DSM. These contours were clipped at the maximum extent of quarry

boundaries traced from the 1946 orthophoto (Supplementary Figs. 8 and 9). Using the 1846–1857 map as a reference for general relief representation and taking into consideration the geomorphologic features (Rhône river escarpment, drainage, and ridgelines) of the area around the quarry, contours were traced manually in order to fill the blank area and reconstruct the 1833 relief. By assuming for the reconstructed topographic height an uncertainty of 10 m over the whole quarry area as of 1946 ($\sim 300,000 \text{ m}^2$), the uncertainty in the volume removed in the period 1833–1946 (larger than $11,000,000 \text{ m}^3$) deriving from the procedure of reconstruction of the initial topography would be $<30\%$.

Starting from the evolution of the topography, we estimated the volume of the mass progressively removed from the quarry. Instead of comparing the first and last DSM available, in order to increase coherency and avoid very large outliers we split the analysis into intervals: 1833–1946, 1946–1979, 1979–2007, and 2007–2011. Original DSM raster files were clipped and resampled into a common pixel size (3 m) and then converted into point clouds. Point clouds were co-registered using the ICP matching tool from CloudCompare software (<http://www.danielgm.net/cc>; last accessed April 2020) and then each pair was processed with the Multiscale Model to Model Cloud Comparison (M3C2). This technique computes the local distance between two-point clouds along the normal surface direction which tracks 3D variations in surface orientation³⁶. M3C2 distance raster files were cropped using the quarry boundary traced manually from orthophoto maps for each period, and removed volume (Supplementary Table 4). The uncertainty in the determination of the removed volume for each period is also reported) was calculated using raster statistics.

Boussinesq's solution of 3-D elastostatic loading. We adopted the analytic solution in Cartesian coordinates (x_1, x_2, x_3) of the three-dimensional elastostatics for the response of a semi-infinite solid ($x_3 \geq 0$) to an arbitrary normal load P_0 on its boundary³⁷. We considered the displacements and the stress components given the shear modulus μ and the Poisson ratio ν . If P_0 is applied at (x_{01}, x_{02}, x_3) then the displacement components in a generic point (x_1, x_2, x_3) are given by:

$$u_1 = \frac{P_0}{4\pi\mu} \frac{(x_1 - x_{01})}{R} \left[\frac{x_3}{R^2} - (1 - 2\nu) \frac{1}{R + x_3} \right],$$

$$u_2 = \frac{P_0}{4\pi\mu} \frac{(x_1 - x_{02})}{R} \left[\frac{x_3}{R^2} - (1 - 2\nu) \frac{1}{R + x_3} \right],$$

$$u_3 = \frac{P_0}{4\pi\mu R} \left[\frac{x_3^2}{R^2} + 2(1 - \nu) \right],$$

where $R = \sqrt{(x_1 - x_{01})^2 + (x_2 - x_{02})^2 + x_3^2}$. The components of the displacement can be used to compute the strain tensor ϵ and the stress tensor σ in the same point (x_1, x_2, x_3). Under the hypothesis of infinitesimal deformation and for isotropic medium, $\epsilon_{ij} = 1/2(dU_j/dx_i + dU_i/dx_j)$ and $\sigma_{ij} = \lambda\delta_{ij}\epsilon_{kk} + 2\mu\epsilon_{ij}$, where λ is the second Lamé's parameter and δ_{ij} the Kronecker delta. In particular, for the application presented in this study we used the six components of the stress tensor, which have the following expressions:

$$\sigma_{11} = -\frac{P_0}{2\pi R^2} \left\{ \frac{3(x_1 - x_{01})^2 x_3}{R^3} - (1 - 2\nu) \left[\frac{x_3}{R} - \frac{R}{R + x_3} + \frac{(x_1 - x_{01})^2 (2R + x_3)}{R(R + x_3)^2} \right] \right\},$$

$$\sigma_{22} = -\frac{P_0}{2\pi R^2} \left\{ \frac{3(x_2 - x_{02})^2 x_3}{R^3} - (1 - 2\nu) \left[\frac{x_3}{R} - \frac{R}{R + x_3} + \frac{(x_2 - x_{02})^2 (2R + x_3)}{R(R + x_3)^2} \right] \right\},$$

$$\sigma_{12} = -\frac{P_0}{2\pi R^2} (x_1 - x_{01})(x_2 - x_{02}) \left[\frac{3x_3}{R^3} - (1 - 2\nu) \frac{(2R + x_3)}{R(R + x_3)^2} \right],$$

$$\sigma_{13} = -\frac{3P_0}{2\pi R^5} (x_1 - x_{01})x_3^2,$$

$$\sigma_{23} = -\frac{3P_0}{2\pi R^5} (x_2 - x_{02})x_3^2,$$

$$\sigma_{33} = -\frac{3P_0}{2\pi R^5} x_3^2.$$

In order to quantify the effect of the removal of the rock mass from the quarry on the prescribed fault, we assumed that extraction operation is equivalent to the application of a set of vertical forces $P_0 = h dA \cdot \rho \cdot g$ (being h the height of the eroded rock column computed from the DEM, ρ the rock density, g the acceleration of gravity and dA the elementary area of the DEM), at the surface of the investigated volume. Given the linearity of the model, the net effect on the fault in terms of σ_{ij} is obtained by summing the contributions of the single forces. By decomposing σ_{ij} in its normal component $\Delta\sigma_n$ (assumed positive if the fault is unclamped) and shear component $\Delta\tau$ (assumed positive in the direction of the slip) along the fault and assuming a given value of the fault effective friction coefficient μ' we computed the Coulomb stress change $\Delta\text{CFF} = \Delta\tau + \mu' \Delta\sigma_n$. Specifically, we investigated three values of $\mu' = 0.4, 0.5, 0.6$ (Supplementary Fig. 10), generally assumed as plausible

effective friction coefficient for natural faults^{38,39} and minor differences resulted in the maximum values, while no change in the general Δ CFF pattern. Conservatively, in order to estimate the effect of the quarry activity on the faults associated with the Le Teil earthquake, we used the results for $\mu = 0.4$ (Fig. 3c), associated with the lower maximum value.

Data availability

The photogrammetric point cloud used in this study is available in the OpenTopography repository, <https://doi.org/10.5069/G9BC3WQ4>, while all the other datasets generated during and/or analyzed during the current study are available in the Zenodo repository, <https://doi.org/10.5281/zenodo.3973027>.

Code availability

All the custom codes used in this study are available from the V.D.N. (email: denovellis.v@irea.cnr.it) on request.

Received: 20 April 2020; Accepted: 18 August 2020;

Published online: 18 September 2020

References

- Grigoli, F. et al. The November 2017 MW 5.5 Pohang earthquake: a possible case of induced seismicity in South Korea. *Science* **360**, 1003–1006 (2018).
- Foulger, G. R., Wilson, M. P., Gluyas, J. G., Julian, B. R. & Davies, R. J. Global review of human-induced earthquakes. *Earth-Sci. Rev.* **178**, 438–514 (2018).
- Dahm, T. et al. Recommendation for the discrimination of human-related and natural seismicity. *J. Seismol.* **17**, 197–202 (2013).
- Deichmann, N. & Giardini, D. Earthquakes induced by the stimulation of an enhanced geothermal system below Basel (Switzerland). *Seismol. Res. Lett.* **80**, 784–798 (2009).
- Ellsworth, W. L. Injection-induced earthquakes. *Science* **341**, 1225942 (2013).
- Amos, C. B. et al. Uplift and seismicity driven by groundwater depletion in central California. *Nature* **509**, 483–486 (2014).
- Lei, X. et al. Fault reactivation and earthquakes with magnitudes of up to MW 4.7 induced by shale-gas hydraulic fracturing in Sichuan Basin, China. *Sci. Rep.* **7**, 7971 (2017).
- González, P. J., Tiampo, K. F., Palano, M., Cannavò, F. & Fernandez, J. The 2011 Lorca earthquake slip distribution controlled by groundwater crustal unloading. *Nat. Geosci.* **5**, 821–825 (2012).
- Klose, C. D. Mechanical and statistical evidence of the causality of human-made mass shifts on the Earth's upper crust and the occurrence of earthquakes. *J. Seismol.* **17**, 109–135 (2013).
- Qian, Y. et al. An extremely shallow MW4.1 thrust earthquake in the eastern Sichuan Basin (China) likely triggered by unloading during infrastructure construction. *Geophys. Res. Lett.* **46**, 13775–13784 (2019).
- Elmi, S. et al. Notice explicative de la carte géologique de France (1/50000), Feuille Aubenas (865) (Edition du BRGM, Orléans, 1996).
- Saint Martin, M. Carte géologique harmonisée du département de l'Ardèche notice technique (BRGM7RP-57097-FR, Bureau de Recherches Géologiques et Minières, 2009).
- Hannouz, E. et al. Geomorphology of the cumulative deformation since Oligocene age on the Mw 4.9 Le Teil earthquake fault (South of France, 11/11/19), EGU General Assembly 2020, Online, 4–8 May 2020, EGU2020-20740, <https://doi.org/10.5194/egusphere-egu2020-20740> (2020).
- Thouvenot, T. et al. The ML 5.3 Épagny (French Alps) earthquake of 1996 July 15: a long-awaited event on the Vuache Fault. *Geophys. J. Int.* **35**, 876–892 (1998).
- Tesauro, M., Hollenstein, C., Egli, R., Geiger, A. & Kahle, H.-G. Analysis of central western Europe deformation using GPS and seismic data. *J. Geodyn.* **42**, 194–209 (2006).
- Nguyen, H. N., Vernant, P., Mazzotti, S., Khazaradze, G. & Asensio, E. 3D GPS velocity field and its implications on the present-day post-orogenic deformation of the Western Alps and Pyrenees. *Solid Earth* **7**, 1349–1363 (2016).
- Masson, C., Mazzotti, S., Vernant, P. & Doerflinger, E. Extracting small deformation beyond individual station precision from dense Global Navigation Satellite System (GNSS) networks in France and western Europe. *Solid Earth* **10**, 1905–1920 (2019).
- Ritz, J.-F., et al. The Mw4.9 Le Teil surface-rupturing earthquake in southern France: new insight on seismic hazard assessment in stable continental regions, EGU General Assembly 2020, Online, 4–8 May 2020, EGU2020-8409, <https://doi.org/10.5194/egusphere-egu2020-8409> (2020).
- Okada, Y. Internal deformation due to shear and tensile faults in a half-space. *Bull. Seismol. Soc. Am.* **82**, 1018–1040 (1992).
- Davis, S. D. & Frohlich, C. Did (or will) fluid injection cause earthquakes? Criteria for a rational assessment. *Seismol. Res. Lett.* **64**, 207–224 (1993).
- S. Hirschberger, S. Wiemer, P. Burgherr, Eds., Energy from the Earth. Deep geothermal as resource for the future (TA-Swiss, vdf Hochschulverlag AG, Zürich, 2015).
- Pino, N. A., Convertito, V. & Madariaga, R. Clock advance and magnitude limitation through fault interaction: the case of the 2016 central Italy earthquake sequence. *Sci. Rep.* **9**, 5005 (2019).
- Wang, S. et al. Changes in groundwater level possibly encourage shallow earthquakes in central Australia: The 2016 Petermann Ranges earthquake. *Geophys. Res. Lett.* **46**, 3189–3198 (2019).
- Costantini, M. A novel phase unwrapping method based on network programming. *IEEE Trans. Geosci. Remote Sens.* **36**, 813–821 (1998).
- Atzori, S., Manunta, M. & Fornaro, G., & Athanassios Ganas, S. Salvi. Postseismic displacement of the 1999 Athens earthquake retrieved by the differential interferometry by synthetic aperture radar time series. *J. Geophys. Res.* **133**, B09309 (2008).
- Williams, C. A. & Wadge, G. An accurate and efficient method for including the effects of topography in three-dimensional elastic models of ground deformation with applications to radar interferometry. *J. Geophys. Res.* **105**, 8103–8120 (2000).
- Ben-Menahem, A. Radiation of seismic surface waves from finite moving sources. *Bull. Seism. Soc. Am.* **51**, 401–453 (1961).
- Joyner, W. B. Directivity for non-uniform ruptures. *Bull. Seismol. Soc. Am.* **81**, 1391–1395 (1991).
- Boatwright, J. The persistence of directivity in small earthquakes. *Bull. Seismol. Soc. Am.* **97**, 1850–1861 (2007).
- Convertito, V., Pino, N. A. & Di, F. Luccio, Investigating source directivity of moderate earthquakes by multiple approach: the 2013 Matese (southern Italy) $M_w = 5$ event. *Geophys. J. Int.* **207**, 1513–1528 (2016).
- Brune, J. N. Tectonic stress and the spectra of seismic shear waves from earthquakes. *J. Geophys. Res.* **75**, 4997–5009 (1970).
- Aki, K. & Richards, P. G. *Quantitative seismology*. (University Science, Sausalito, CA, 2002).
- Prieto, G. A., Thomson, D. J., Vernon, F. L., Shearer, P. M. & Parker, R. L. Confidence intervals for earthquake source parameters. *Geophys. J. Int.* **168**, 1227–1234 (2007).
- Rupnik, E., Daakir, M. & Deseilligny, M. Pierrot. MicMac—a free, open-source solution for photogrammetry. *Open Geospatial Data Softw. Stand* **2**, 14 (2017).
- Favre, C., et al. Digitalisation des cartes anciennes. Manuel pour la vectorisation de l'usage des sols et le géoréférencement des minutes 1:40 000 de la carte d'états-major, Version 12.8, INRA (http://docs.gip-ecofor.org/public/forets_ancienne/Manuel_digitalisation_EM_Favre_et_al_2016_v12.8.pdf; 2016).
- Lague, D., Brodu, N. & Leroux, J. Accurate 3D comparison of complex topography with terrestrial laser scanner: application to the Rangitikei canyon (N-Z). *ISPRS J. Photogram. Remote Sens.* **82**, 10–26 (2013).
- Hetnarski, R. B. & Ignaczak, J. *The mathematical theory of elasticity*. (CRC Press Taylor & Francis Group, Boca Raton, FL, 2011).
- King, G. C., Stein, R. S. & Lin, J. Static stress changes and the triggering of earthquakes. *Bull. Seismol. Soc. Am.* **84**, 935–953 (1994).
- Toda, S., Stein, R. S., Reasenber, P. A., Dieterich, J. H. & Yoshida, A. Stress transferred by the 1995 Mw= 6.9 Kobe, Japan, shock: effect on aftershocks and future earthquake probabilities. *J. Geophys. Res.* **103**, 24543–24565 (1998).

Acknowledgements

The authors thank E. Valerio for her contribution to geodetic data analysis and modeling and S. Atzori for fruitful discussions on the geodetic inversion procedure. This work was partially funded by the PRIN project MATISSE (Bando 2017, Prot. 20177EPPN2), the EPOS-SP project (GA 871121), the I-AMICA (PONA3_00363) project, and the 2019–2021 IREA-CNR and Italian Civil Protection Department (DPC) agreement. As for this latter and the IREA-CNR authors, this paper represents the authors' ideas and does not necessarily corresponds to the official opinion and policies of DPC.

Author contributions

V.C., V.D.N., and N.A.P. conceived the study, interpreted the results, and wrote the paper, with contribution from S.V.; R.L., F.C., and M.F.M.T. analyzed the DInSAR data; V.D.N. inverted the geodetic data; S.V. performed the analyses relative to the estimate of the volume removed from the quarry; V.C. and N.A.P. performed Coulomb stress and rupture directivity analyses. All the authors contributed to review the paper.

Competing interests

The authors declare no competing interests.

Additional information

Supplementary information is available for this paper at <https://doi.org/10.1038/s43247-020-00021-6>.

Correspondence and requests for materials should be addressed to N.A.P.

Peer review information Primary handling editor Joe Aslin

Reprints and permission information is available at <http://www.nature.com/reprints>

Publisher's note Springer Nature remains neutral with regard to jurisdictional claims in published maps and institutional affiliations.



Open Access This article is licensed under a Creative Commons Attribution 4.0 International License, which permits use, sharing, adaptation, distribution and reproduction in any medium or format, as long as you give appropriate credit to the original author(s) and the source, provide a link to the Creative Commons license, and indicate if changes were made. The images or other third party material in this article are included in the article's Creative Commons license, unless indicated otherwise in a credit line to the material. If material is not included in the article's Creative Commons license and your intended use is not permitted by statutory regulation or exceeds the permitted use, you will need to obtain permission directly from the copyright holder. To view a copy of this license, visit <http://creativecommons.org/licenses/by/4.0/>.

© The Author(s) 2020, corrected publication 2021

Supplementary Information

Coincident locations of rupture nucleation during the 2019 Le Teil earthquake, France and maximum stress change from local cement quarrying

Vincenzo De Novellis¹, Vincenzo Convertito², Sotiris Valkaniotis³, Francesco Casu¹, Riccardo Lanari¹, Mario Fernando Monterroso Tobar¹, Nicola Alessandro Pino^{2,*}

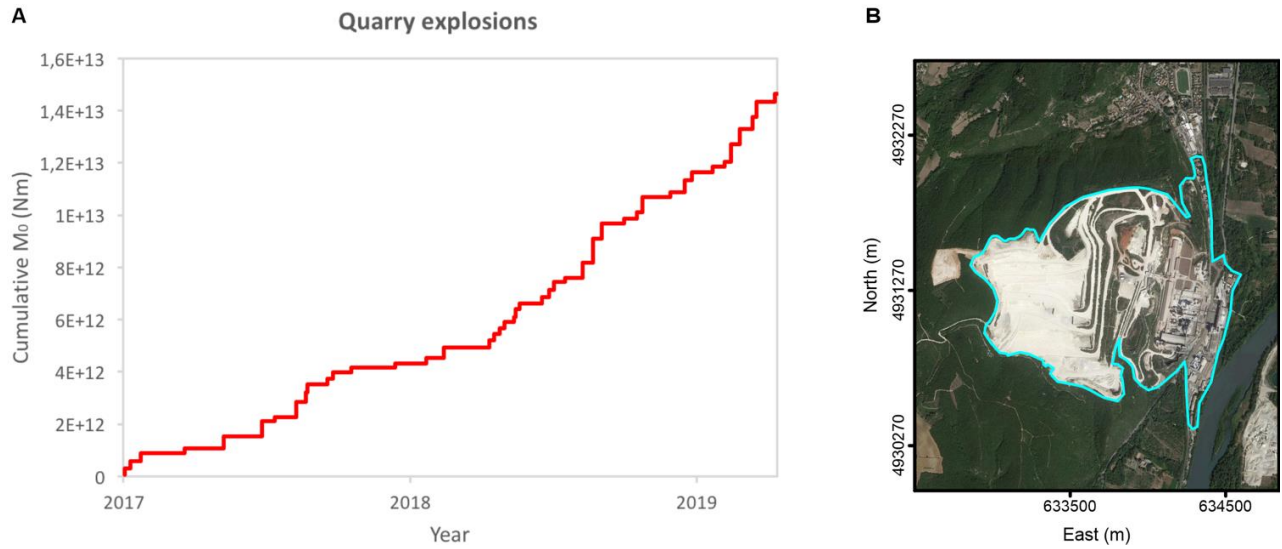
¹Consiglio Nazionale delle Ricerche, Istituto per il Rilevamento Elettromagnetico dell'Ambiente, Napoli, Italy.

²Istituto Nazionale di Geofisica e Vulcanologia, Osservatorio Vesuviano, Napoli, Italy.

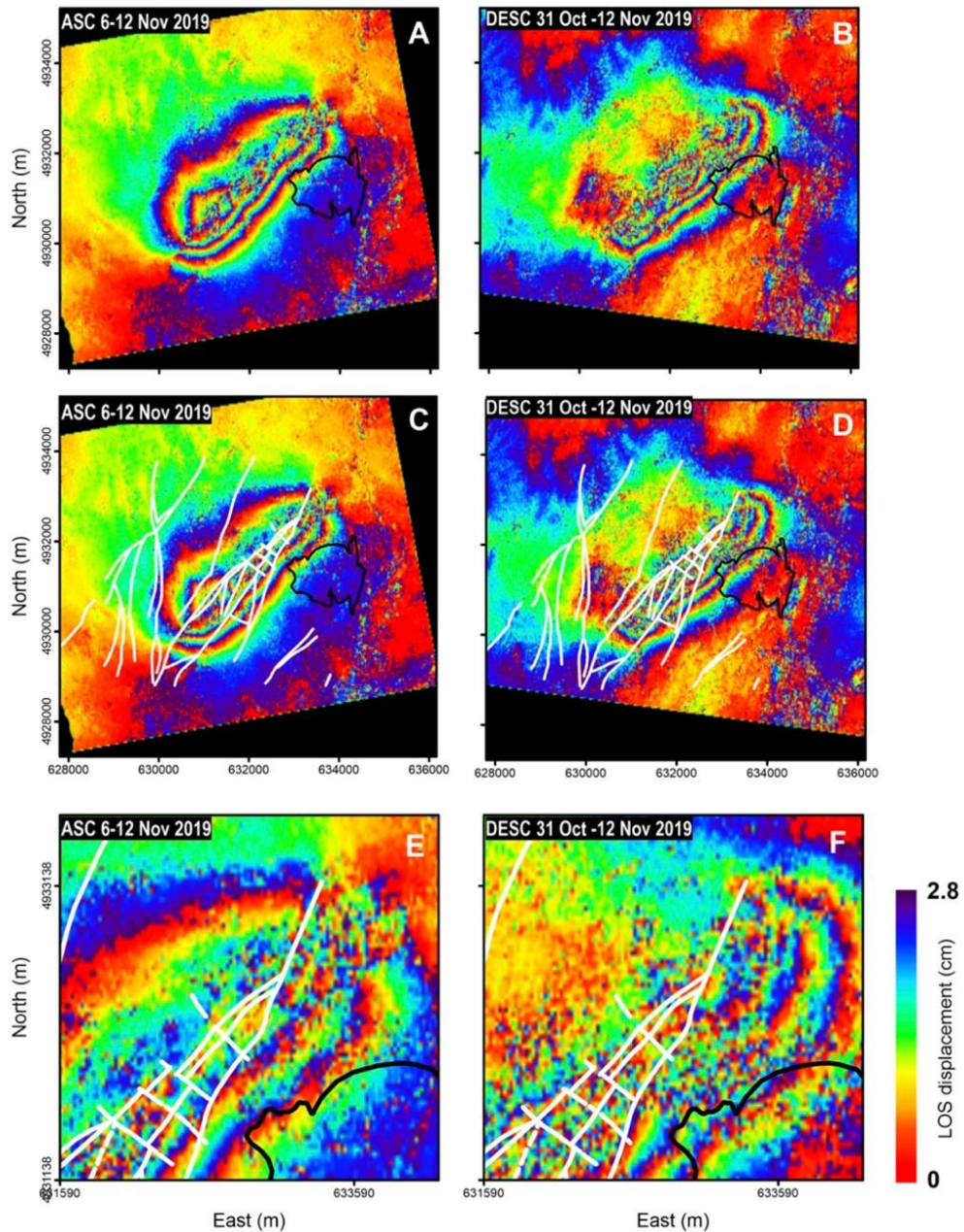
³Koronidos Str., 42131 Trikala, Greece.

*Corresponding author. Email: alessandro.pino@ingv.it

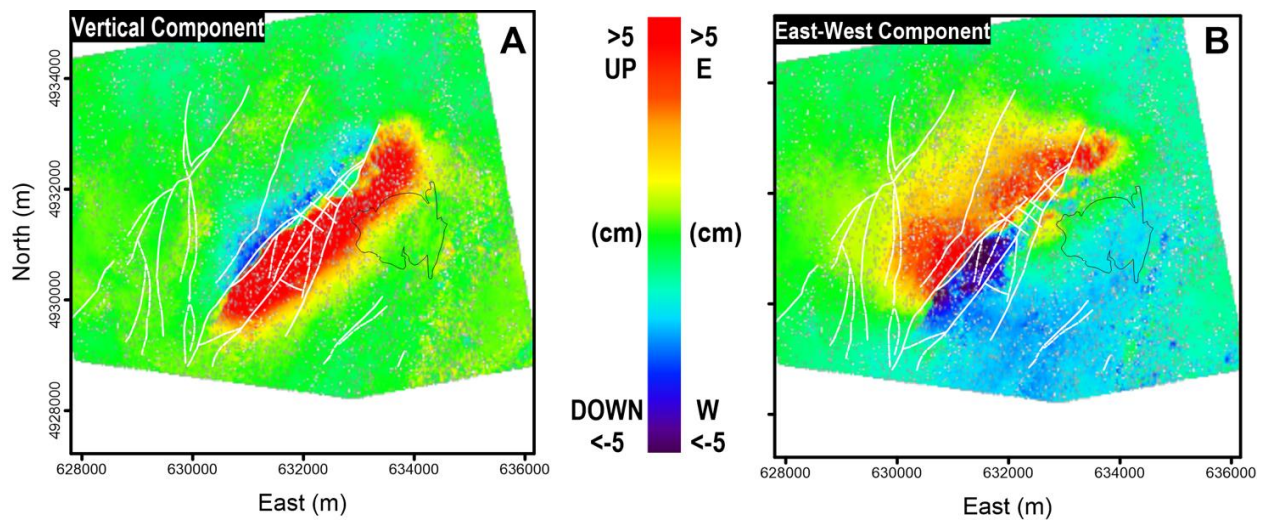
Supplementary Figures



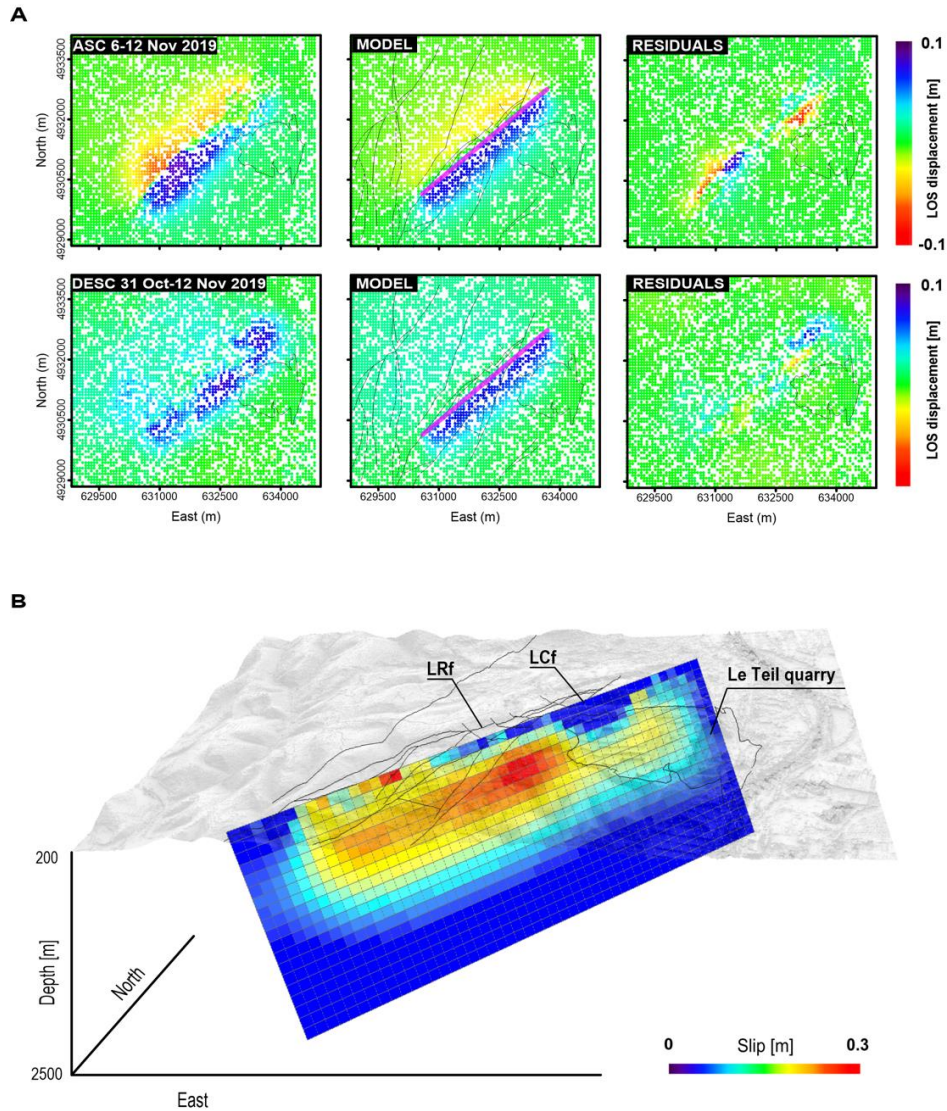
Supplementary Fig. 1. Clues to the Le Teil quarry activity post 2011. (A) Cumulative seismic moment released by blasts in the $10 \times 10 \text{ km}^2$ area centered on the Le Teil quarry, from August 2, 2017 to November 11, 2019. For each event, the seismic moment is computed from M_W as obtained from the correspondence M_L - M_W , derived for small earthquake ($M < 3.1$) in France¹. (B) Aerial image of the Le Teil quarry area taken on August 25, 2018, with a contour of the extraction area as of 2011 (cyan).



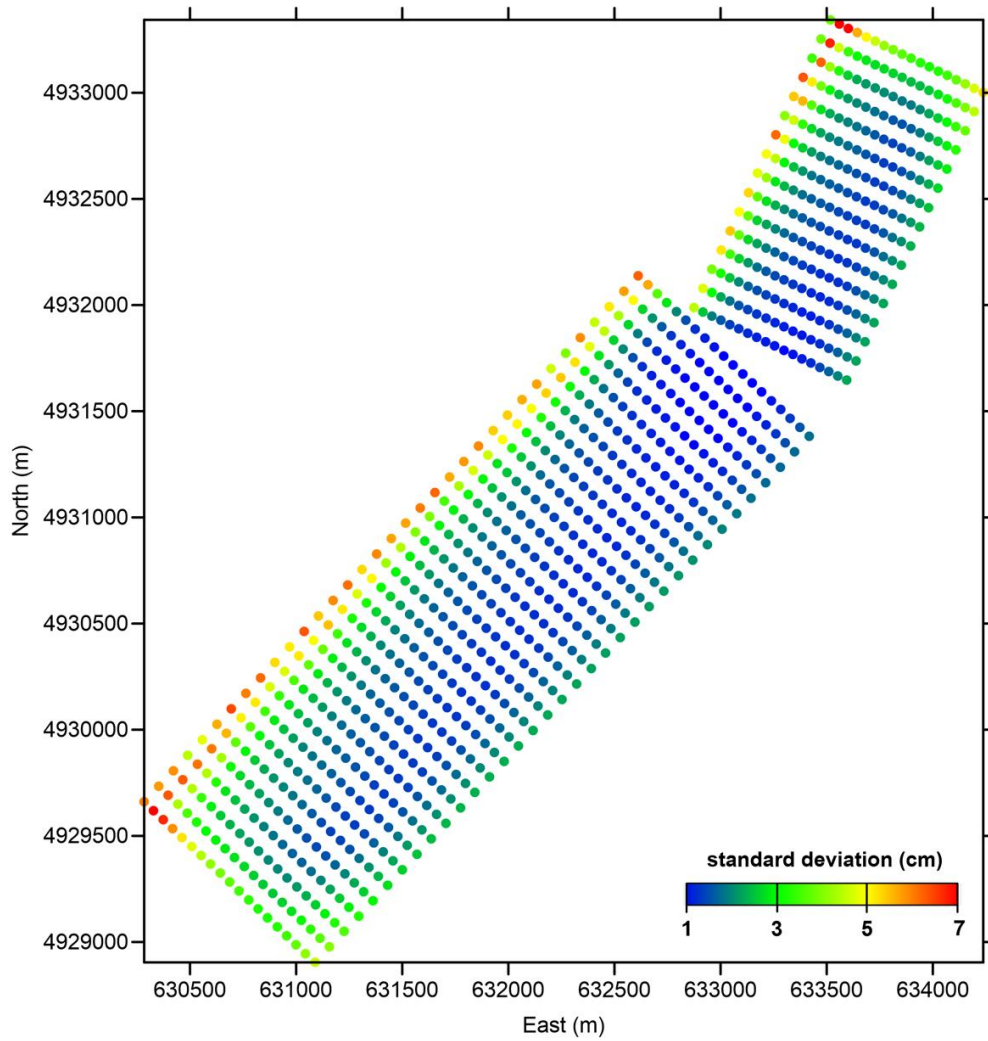
Supplementary Fig. 2. Differential interferometric synthetic aperture radar analysis. LOS interferograms generated from Sentinel-1 image data pairs acquired on 6-12 November 2019 and 31 October-12 November 2019 and selected for the geodetic modeling. (A) wrapped ascending and (B) wrapped descending maps. (C) and (D) same as (A) and (B) with the principal geological structures² superimposed as white lines. (E) and (F) enlargement of (C) and (D), focused on the area of the La Chade Hill's NW flank. In all the panels the black close contour outlines the Le Teil quarry area, as of 2011.



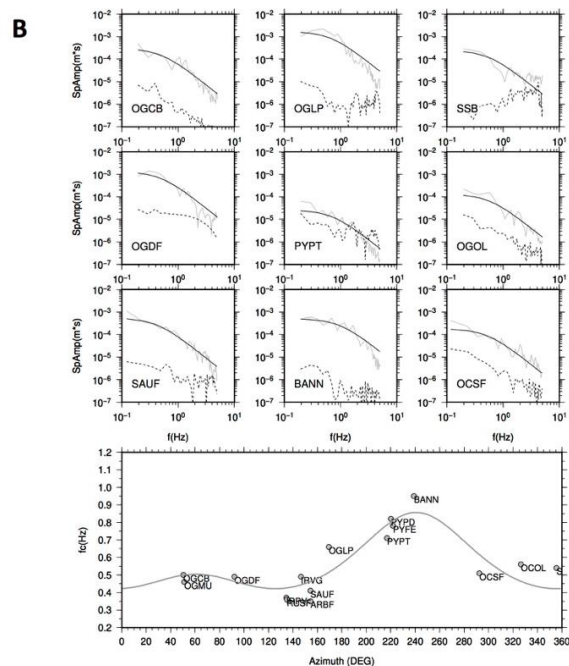
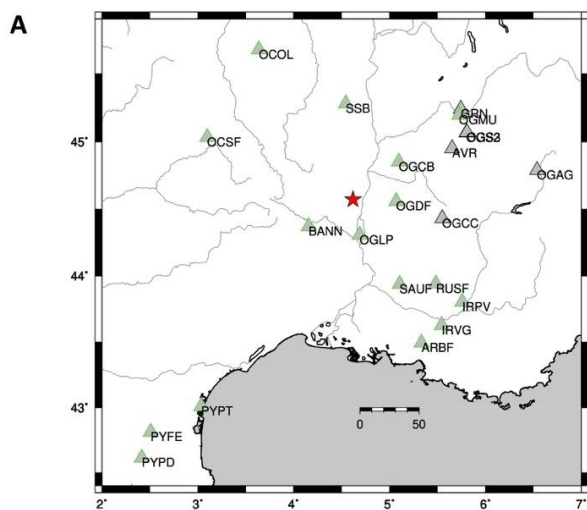
Supplementary Fig. 3. Sentinel-1 DInSAR measurements. (A) Vertical and (B) East-West displacement maps obtained through the combination of the geocoded displacement maps computed by exploiting the ascending and descending Sentinel-1 measurements shown in Fig. 2. In both panels the black close contour outlines the Le Teil quarry area, as of 2011.



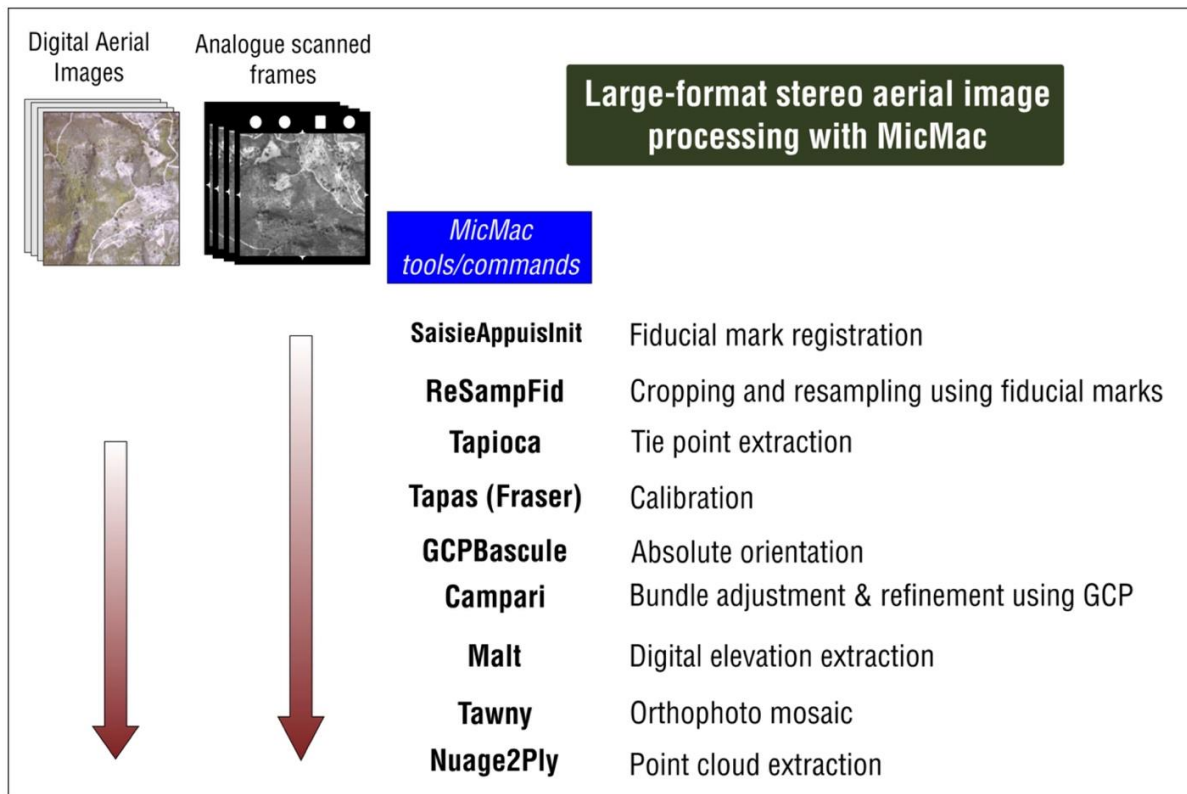
Supplementary Fig. 4. Modeling of ground deformation data with a single fault plane. (A) LOS projected displacement maps for S1 ascending and descending orbits interferograms (left) and predicted LOS projected displacement maps, computed from the retrieved analytical model for the S1 ascending and descending orbits interferograms (center). Their corresponding residual maps are also shown (right). The magenta line indicates the trace of the retrieved fault plane. (B) The retrieved fault plane with distributed slip displayed in perspective view. LRf and LCf indicate the La Rouviere and La Chade faults, respectively (see text). In both panels, the black lines correspond to the principal geological structures in the source area², while the black close contour outlines the quarry area as of 2011.



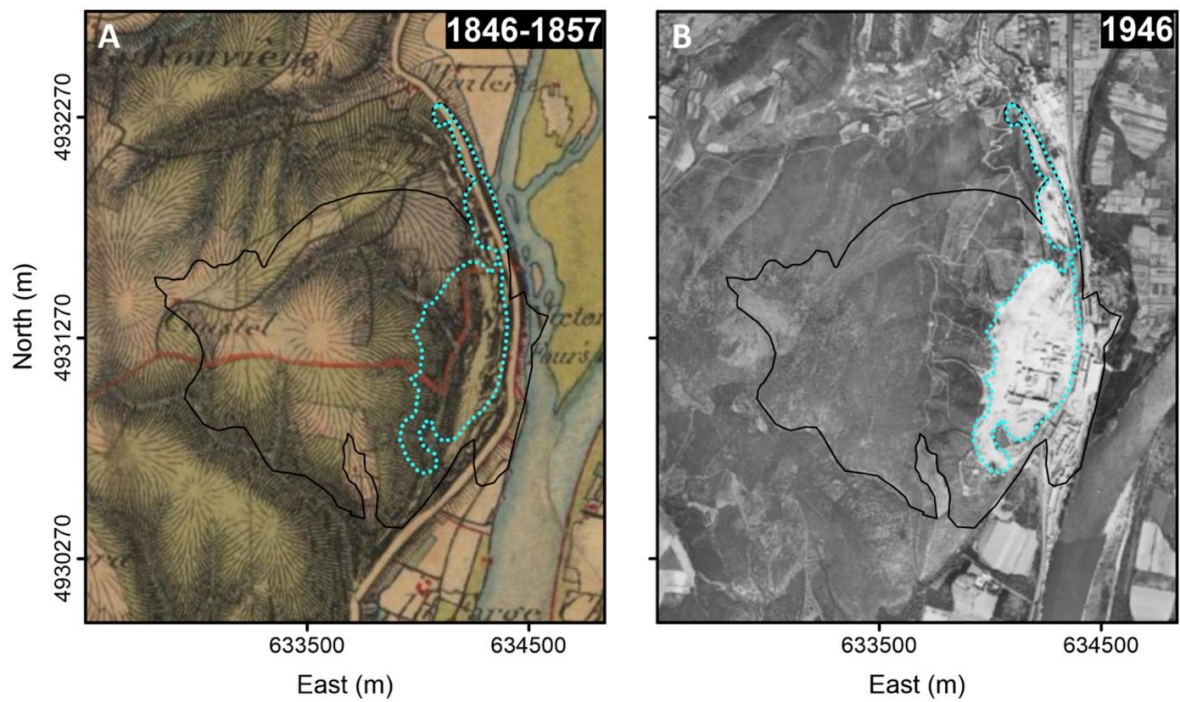
Supplementary Fig. 5. Standard deviation associated with the preferred solution for the slip distribution. Plain view of the standard deviation associated with the slip values obtained for the two-fault solution illustrated in Fig. 2B.



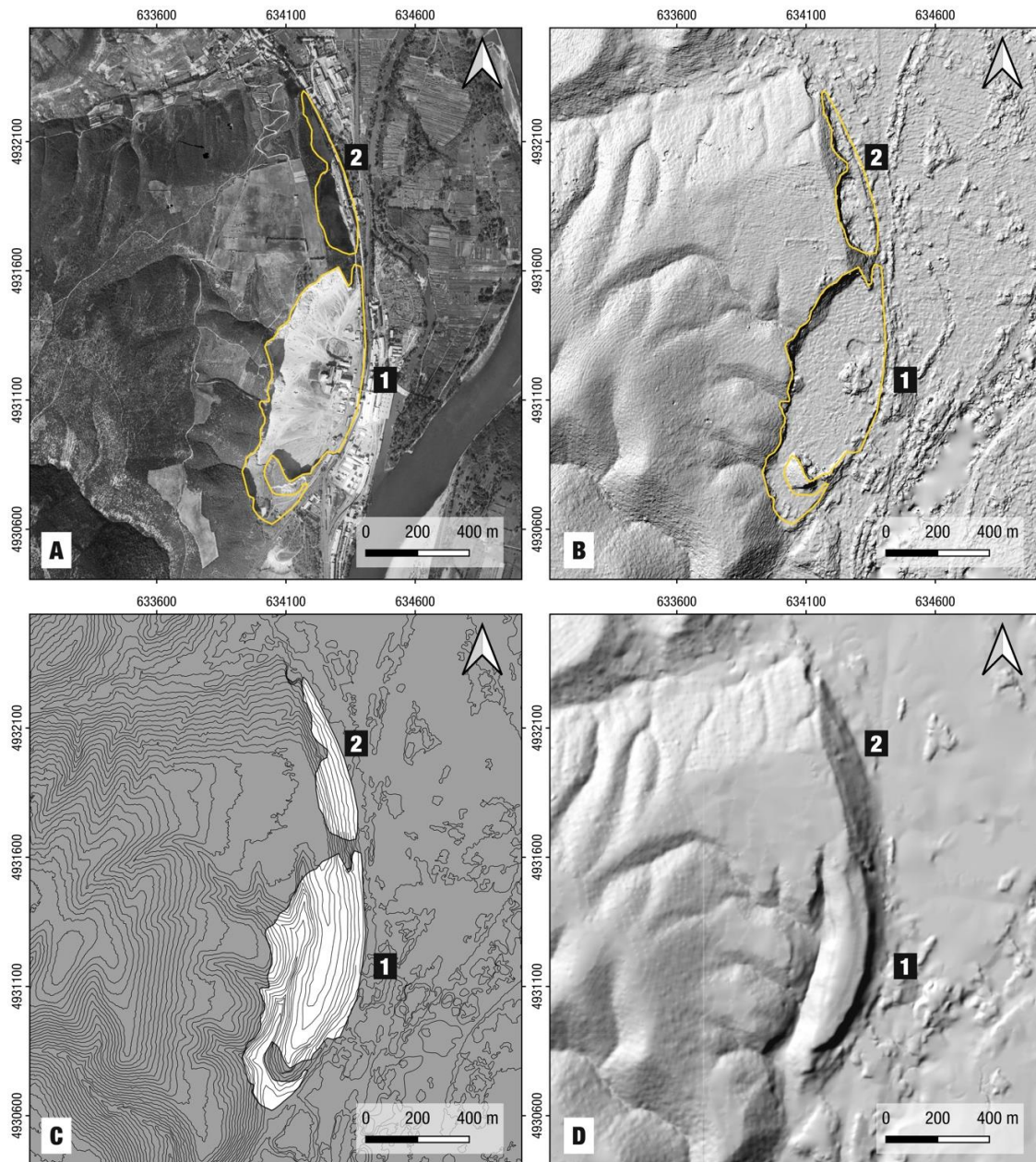
Supplementary Fig. 6. Source directivity analysis. (A) Geographic distribution of the stations used to analyse source directivity effects from the source spectrum corner frequencies. The red star identifies the epicenter of the Le Teil earthquake. The grey triangles with black border indicate the stations discarded from the analysis due to poor signal-to-noise ratio. (B) The upper panels show the observed (grey lines) displacement spectra, the noise spectra (dashed lines), and the best model at a set of representative stations whose location is reported in panel (A). The lower panel shows the estimated corner frequency at each station as a function of the azimuth. The grey curve represents the best C_d function.



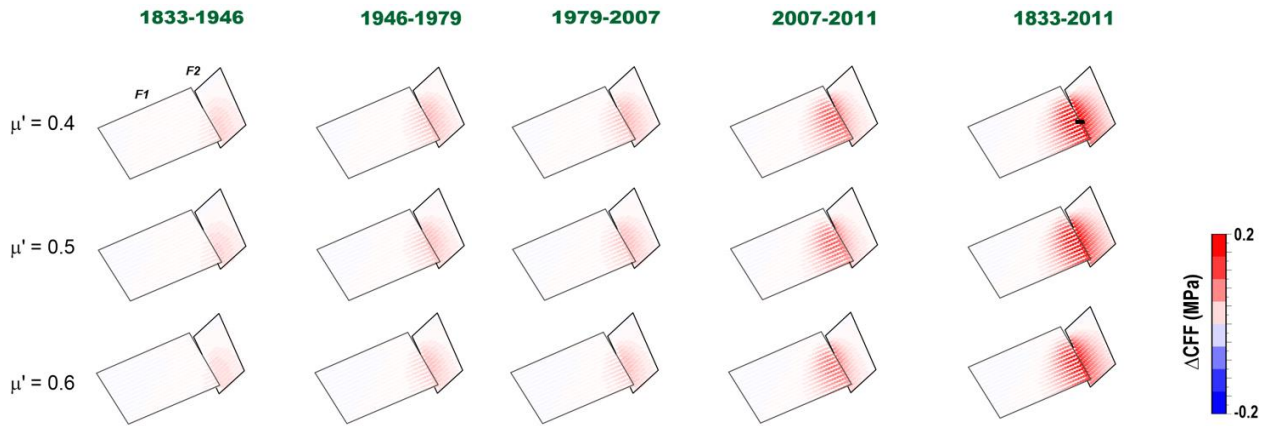
Supplementary Fig. 7. MicMac software workflow. Steps in stereo aerial imagery processing for Digital Surface Model production, using MicMac software³.



Supplementary Fig. 8. Estimate of the initial reference topography. (A) Historical topographic map of the Le Teil quarry area (mapping between 1846 and 1857). Although the map provides no absolute elevation data for the site, it offers an insight of the pre-quarry natural relief. Reconstructed area is shown with cyan dotted contours. (B) 1946 orthophoto map of the same area, used to calibrate the initial topography. In both panels, the black line outlines the 2011 quarry area.



Supplementary Fig. 9. Reconstruction of 1833 topography. (A) Quarry areas are identified and traced using the 1946 orthophotomap. Area 1 represents the main quarry and cement production facility; area 2 represents smaller quarries inactive during 1946. (B) 1946 relief with excavated and modified areas 1 and 2. (C) Generated contour lines from the 1946 digital elevation model. Contour lines in the white areas (1 and 2) were deleted and new ones were manually traced based on the 1857 map, following the main relief features (Rhône river escarpment, drainage and ridgelines). (D) Reconstructed 1833 relief from modified contour lines.



Supplementary Fig. 10. Effect of the Le Teil quarry activity. Coulomb stress change caused by the rock extraction, for each selected time interval and total, on the faults associated with the Le Teil earthquake, for three different values of the effective friction coefficient μ' . The small black square (in the upper right panel) indicates the point where the ΔCFF values in the Supplementary Table 4 are computed.

Supplementary Tables

Supplementary Table 1. Fault geometry of the preferred solutions for the geodetic inversion, for single fault and two faults solutions.

	Depth range (m)	Dip (°)	Strike (°)	Rake (°)	Max. slip (m)	Southern end (UTM)	Northern end (UTM)	Length (m)	Width (m)
Single Fault	-200 1400	62.3	50.0	116.5	0.26	630261 4929215	632553 4933006	5000	1900
Two faults - F1	-240 1190	52.2	43.2	98.0	0.29	630284 4928904	633418 4932138	3500	1900
Two faults - F2	-177 1325	62.0	25.4	93.4	0.21	632874 4931646	634238 4933344	1600	1900

Supplementary Table 2. Main characteristics of the generated interferometric pairs. The seismic sources were retrieved from pairs indicated with (*).

Sensor	DInSAR pair	Orbit	Perpendicular baseline (m)	Track
Sentinel-1	31102019-12112019	ASC	-14.4	59
Sentinel-1	06112019-12112019*	ASC	-15.2	59
Sentinel-1	06112019-18112019	ASC	105.4	59
Sentinel-1	31102019-12112019*	DESC	-75.7	139
Sentinel-1	06112019-12112019	DESC	-53.9	139
Sentinel-1	06112019-18112019	DESC	-13.1	139

Supplementary Table 3. IGN stereo aerial imagery used for digital surface model extraction.
The values with (*) indicate a digital aerial camera format, metadata contain only ground resolution value.

Date	Flight ID	Scale
08/10/1946	C3036-0051_1946_F3036-3038_0611	1/22,000
13/08/1979	C0145-2641_1979_F3-18-12_0424	1/15,000
26/07/2007	CP07000142_FD0007x016_0644	79cm*
16/04/2011	CP11000162_FD07x00033_00979	50cm*

Supplementary Table 4. Digital surface model changes for the Le Teil quarry.

Time period	Volume removed (m ³)	Mean annual removed volume (m ³ /yr)	Δ CFF* (MPa)
1833-1946	11,335,817±306,167	100,316±2,709	0.02
1946-1979	8,290,294±628,418	251,221±19,043	0.04
1979-2007	18,511,103±842,939	661,111±30,105	0.11
2007-2011	4,139,120±479,144	1,034,780±119,786	0.03
1833-2011	42,276,334	237,507	0.19

* Δ CFF is computed at the point indicated in Supplementary Fig. 10

References

1. M. Cara et al., SI-Hex: a new catalogue of instrumental seismicity for metropolitan France. *Bull. Soc. Geol. France* **186**, 3-19 (2015).
2. M. Saint Martin, *Carte géologique harmonisée du département de l'Ardèche notice technique* (BRGM7RP-57097-FR, Bureau de Recherches Géologiques et Minières, 2009).
3. E. Rupnik, M. Daakir, M. Pierrot Deseilligny, MicMac – a free, open-source solution for photogrammetry. *Open geospatial data, softw. stand.* **2**, 14 (2017).